Acta Astronautica 128 (2016) 107–118

Contents lists available at ScienceDirect

Acta Astronautica

journal homepage: www.elsevier.com/locate/aa

# Tip-to-tail numerical simulation of a hypersonic air-breathing engine with ethylene fuel

Malsur Dharavath, P. Manna, Debasis Chakraborty *

*Scientist, Directorate of Computational Dynamics, Defence Research and Development Laboratory, Kanchanbagh, Hyderabad 500058, India*

ARTICLE INFO

*Article history:*
Received 19 February 2016
Received in revised form
29 June 2016
Accepted 7 July 2016
Available online 9 July 2016

*Keywords:*
Reacting flow
Scramjet
Hypersonic vehicle
CFD
Combustion efficiency

ABSTRACT

End to end CFD simulations of external and internal flow paths of an ethylene fueled hypersonic air-breathing vehicle with including forebody, horizontal fins, vertical fins, intake, combustor, single expansion ramp nozzle are carried out. The performance of the scramjet combustor and vehicle net thrust-drag is calculated for hypersonic cruise condition. Three-dimensional Navier–Stokes equations are solved along with *SST-k–ω* turbulence model using the commercial CFD software *CFX-14*. Single step chemical reaction based on fast chemistry assumption is used for combustion of gaseous ethylene fuel. Simulations captured complex shock structures including the shocks generated from the vehicle nose and compression ramps, impingement of cowl-shock on vehicle undersurface and its reflection in the intake and combustor etc. Various thermochemical parameters are analyzed and performance parameters are evaluated for nonreacting and reacting cases. Very good mixing (~98%) of fuel with incoming air stream is observed. Positive thrust–drag margins are obtained for fuel equivalence ratio of 0.6 and computed combustion efficiency is observed to be 94 %. Effect of equivalence ratio on the vehicle performance is studied parametrically. Though the combustion efficiency has come down by 8% for fuel equivalence ratio of 0.8, net vehicle thrust is increased by 44%. Heat flux distribution on the various walls of the whole vehicle including combustor is estimated for the isothermal wall condition of 1000 K in reacting flow. Higher local heat flux values are observed at all the leading edges of the vehicle (i.e., nose, wing, fin and cowl leading edges) and strut regions of the combustor.

© 2016 IAA. Published by Elsevier Ltd. All rights reserved.

## 1. Introduction

Hypersonic propulsion can be used very effectively for high-speed transport, national defense, space access etc. and scramjet engine is the preferred choice for such applications. Curran [1] reviewed the scramjet engine development in various countries including United States, Russia, France, Germany, Japan and Australia during 1960–2000. Although, research on scramjet engines started way back in the 1960, flight testing of scramjet-powered airbreathing mission is attempted only in the last decade. Many technical issues need to be addressed before scramjet engines are used in any practical vehicle. Different fuel injection systems namely struts, pylons or cavities [2] are used for scramjet engine. Injection, mixing and burning of fuel within the combustor length are some of the major challenges in the realization of a flight worthy scramjet combustor. For volume limited applications and for $M_\infty < 8$, hydrocarbon fuel has many advantages. Vaporization, mixing and combustion of a kerosene fueled scramjet combustor using struts are studied in detail [3] to deliver the required thrust for a hypersonic flight vehicle. The successful Mach-7 flight test of hydrogen fuelled scramjet powered hypersonic flight vehicle (X-43A) [4,5] and Mach-10 flight of hydrocarbon fuelled scramjet vehicle (X- 51A) [6] in the last decade demonstrated the capability of airframe-integrated scramjet engine and hypersonic air-breathing vehicle design tools. A Hypersonic Flight Experimental Vehicle, (Hyflex) was flight tested [7] in 1996 as the precursor engineering demonstrator of HOPE (H-II Orbiting Plane) program of Japan. The development of a small-scale, 4.2 m long dual-mode scramjet-powered, experimental hypersonic vehicle [8] to demonstrate the capability of prediction of aero-propulsive thrust–drag balance is also reported by MBDA, France and ONERA.

Paneerselvam et al. [9] explained the development of an autonomous operation of a scramjet combustor at hypersonic flight speed (~6.0–6.5) for a flight duration of about 20 s. Although, air launch is an attractive option for hypersonic air-breathing mission by carrying the scramjet integrated vehicle along with the booster to certain altitude using a high powered aircraft followed by acceleration to the desired Mach number by the booster and scramjet engine testing as was done in X-43, ground launch option is considered for the proposed mission. A solid rocket motor

* Corresponding author.
*E-mail address:* debasis_cfd@drdl.drdo.in (D. Chakraborty).

http://dx.doi.org/10.1016/j.actaastro.2016.07.014
0094-5765/© 2016 IAA. Published by Elsevier Ltd. All rights reserved.

booster is being used to carry the scramjet integrated cruise vehicle from ground to the desired altitude and scramjet integrated vehicle would be separated and tested. Liquid kerosene is considered as fuel of the scramjet engine considering the volume limited applications of the mission. The fuel is injected in the incoming air stream through series of struts placed in the combustor flow path to have proper fuel distribution in the whole combustor width. Scramjet combustor configuration was changed in several iterations to meet the requirement of the hypersonic vehicle. Number of ground test in connected pipe mode tests [10,11] and numerical simulations [12,13] were carried out to finalize the number of struts, their positions and fuel injection locations to have benign thermal environment and optimum performance of the flight sized engine.

Ethylene fuel also provides an attractive option for scramjet engine as the injection is performed in gaseous phase and its simpler chemical structure enables easy ignition. Tam et al. [14] proposed optimum strut design from their numerical studies of gaseous ethylene fuel/air mixing characteristics with several strut fuel-injection schemes in Mach 2 inflow condition in a rectangular flow path. Malsur et al. [15] performed three-dimensional reacting simulations for fight worthy scramjet combustor with ethylene fuel injected from a row of struts placed in the flow path for the ground test condition to guide the experimental work. Engine performance in terms of mixing (nonreacting flow with fuel), combustion efficiencies, and thrust is evaluated from simulation results for different fuel equivalence ratio.

Although, CFD tools were used very extensively for the design and analysis of various subsystems of hypersonic airbreathing engine and to understand many complex reacting/non-reacting flow issues like laminar/turbulent transition on forebody, aerothermodymamics, surface heating, high speed combustion etc in hypersonic flight regime; complete vehicle analysis integrating both external and internal flow together is very limited in open literature. For high speed airbreathing system, the vehicle's undersurfaces act as a propulsion device and the aerodynamics and propulsion are so strongly coupled that any demarcation of the subsystem is difficult. The coupled external–internal flow simulations would enable the designer to look at the problem in an integrated way in which thrust minus drag and other performance parameters could be obtained directly from the simulation. Voland et al. [5] reported a tip-to-tail post-test CFD analysis for X-43; but, much detail is not available in the open literature. Malsur et al. [16] carried out an end-to end simulation of a liquid kerosene fueled hypersonic air breathing vehicle with strut based fuel injection system. The simulation demonstrated the positive thrust–drag margin and the computed performance parameters are being used by vehicle designers for mission planning.

In the present work, an integrated reacting-nonreating flow simulation for a hypersonic airbreathing vehicle with gaseous ethylene fuel is performed. Three-dimensional Navier–Stokes equations are solved along with SST-$k$–$\omega$ turbulence model using the commercial CFD software *CFX-14* [17]. Computations are carried out on block structured grid generated by *ICEM-CFD* [18] grid generator package. Infinitely fast rate chemistry is used for combustion modeling. Combustor performance and vehicle aerodynamic parameters are evaluated from the simulation results. Heat flux distribution at various vehicle surface and combustor is also estimated from the integrated simulation considering aerodynamic heating as well as the fuel burning in the combustor.

## 2. Geometrical details of hypersonic vehicle

The schematic of the hypersonic cruise vehicle is shown in Fig. 1. The total length of the vehicle is 7$W$, where $W$ is width of cruise vehicle. There are two ramps placed ahead of the intake entry. The length of the intake is about 1.3$W$ including intake cowl with the cross-sections of $0.7W \times 0.3W$ and $0.7W \times 0.1W$ at the entry and exit respectively. The total length of the combustor is 2.4$W$. The combustor is having varying cross sections. Initially, it has an isolator of 0.1$W$ to reduce the non-uniformity of the intake flow which is followed by divergent sections with three different angles. A solid wall is placed at 0.3$W$ downstream from combustor entry in the middle of the combustor, which makes combustor into two modules. Four struts are provided in each module in such a manner that one module is the mirror image of the other with respect to the middle wall. The struts are straight and cross section remains constant along the height of the combustor are also shown in the same figure. Nine injection holes with 1 mm diameter are provided on either side of the strut to inject the gaseous ethylene fuel inside the combustor. First strut is placed near to the middle wall while 4th strut near to the side wall. The single expansion ramp (*SER*) nozzle with upward divergence angle is attached at the exit of the combustor A bottom nozzle cowl with downward deflection is attached with the bottom wall at exit of the combustor to provide stability and control force for the vehicle.

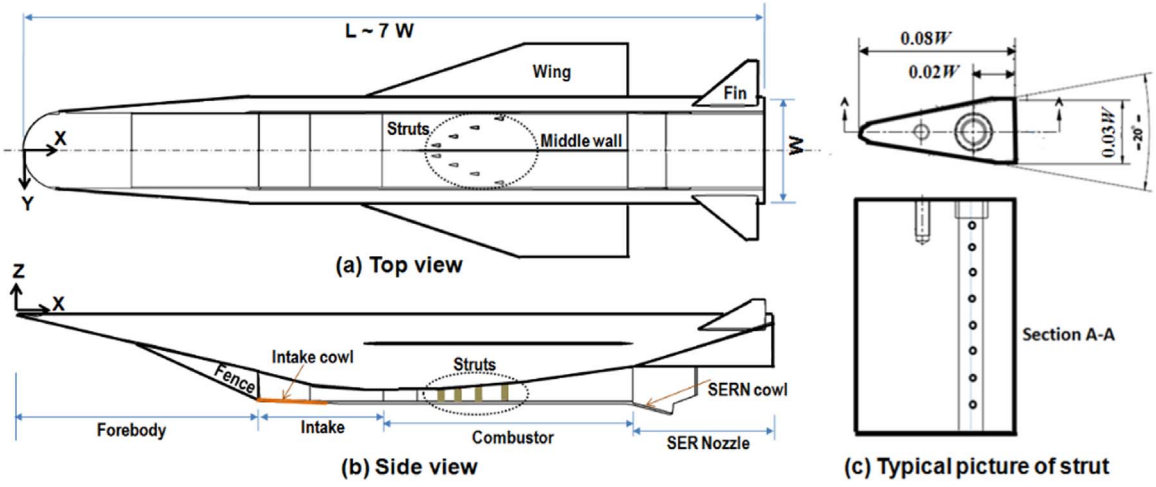


**Fig. 1.** Schematic of hypersonic cruise vehicle with integrated scramjet propulsion system.

## 3. The computational methodology

Commercial CFD software *CFX-14.5* [17] is used for the present analysis. *CFX* is a fully implicit 3D Reynolds Averaged Navier–Stokes (RANS) code, capable of solving diverse and complex turbulent reacting flow problems. *CFX-14.5* implements a general non-orthogonal, structured, boundary fitted grids. The combined combustion model (*CCM*) computes the minimum of the reaction rate of eddy dissipation (*ED*) and finite rate chemistry (*FRM*) models for combustion of ethylene fuel. Turbulence is modeled using *SST-k–ω* turbulence model. Wall functions are used to model flow near the walls. The numerical scheme is 2nd order accurate in space and 1st order accurate in time. Log-normalized maximum residue of fourth order less ($10^{-4}$) is considered as the convergence criteria. The final results is obtained within 10,000 iterations.

### 3.1. Governing equations

The appropriate system of governing equations of mass, momentum, energy, turbulent and species transport equations of an unsteady compressible gas flow may be written as;

*Conservation of mass equation*:

$$\frac{\partial \rho}{\partial t} + \frac{\partial}{\partial x_k}(\rho\ u_k) = 0 \quad k = 1, 2, 3 \tag{1}$$

*Conservation of momentum equation:*

$$\frac{\partial}{\partial t}(\rho\ u_i) + \frac{\partial}{\partial x_k}(\rho\ u_i\ u_k) + \frac{\partial P}{\partial x_i} = \frac{\partial(\tau_{ik})}{\partial x_k}, \quad i, k = 1, 2, 3 \tag{2}$$

*Conservation of energy equation:*

$$\frac{\partial}{\partial t}(\rho\ H) + \frac{\partial}{\partial x_k}(\rho\ u_k H) = -\frac{\partial}{\partial x_k}(u_j\ \tau_{jk}) + \frac{\partial q_k}{\partial x_k}, \quad j, k = 1, 2, 3 \tag{3}$$

*Conservation of species mass fraction ($Y_I$):*

$$\frac{\partial}{\partial t}(\rho\ Y_I) + \frac{\partial}{\partial x_k}(\rho\ u_k Y_I) = \frac{\partial}{\partial x_k}\left(\left(\frac{\mu_l}{\mathrm{Pr}} + \frac{\mu_t}{\sigma_c}\right)\frac{\partial Y_I}{\partial x_k}\right) + \dot{w}_I \tag{4}$$

The rate of production/consumption in Eq. (4), $\dot{w}_I$, for species component *I* can be computed as the sum of the rate of progress for all the elementary reactions in which component *I* participates:

$$\dot{w}_I = M_{wI} \sum_{k=1}^{k} (\nu''_{kI} - \nu'_{kI}) R_k$$

where, $M_{wI}$ is molecular weight of species component *I* and $R_k$ is the elementary reaction rate of progress for reaction, which can be calculated using *CCM*. $\nu''_{kI}$ and $\nu'_{kI}$ are stiochiometric ratio of product and reactant species respectively. More details provided about *CCM* in following sections.

### 3.2. SST-kω turbulence model transport equation

Turbulence closure is achieved by means of Menter's [19] shear stress transport (*SST*) model calibrated for high-speed compressible flows. The model incorporates the standard *k–ε* model that is suitable for shear layer flows and the Wilcox *k–ω* model for wall turbulence effects. Derived from the *k-ε* two equation formulation, the SST model can be written in the following form.

Turbulent kinetic energy (*k*) equation:

$$\frac{\partial}{\partial t}(\rho\ k) + \frac{\partial}{\partial x_k}(\rho\ u_k k) = \frac{\partial}{\partial x_k}\left(\left(\frac{\mu_l}{\mathrm{Pr}} + \frac{\mu_t}{\sigma_k}\right)\frac{\partial k}{\partial x_k}\right) + S_k \tag{5}$$

Turbulent eddy dissipation rate ($\varepsilon$) equation:

$$\frac{\partial}{\partial t}(\rho\ \varepsilon) + \frac{\partial}{\partial x_k}(\rho\ u_k \varepsilon) = \frac{\partial}{\partial x_k}\left(\left(\frac{\mu_l}{\mathrm{Pr}} + \frac{\mu_t}{\sigma_\varepsilon}\right)\frac{\partial \varepsilon}{\partial x_k}\right) + S_\varepsilon \tag{6}$$

*Turbulent frequency rate (ω) equation:*

$$\frac{\partial}{\partial t}(\rho\ \omega) + \frac{\partial}{\partial x_k}(\rho\ u_k \omega) = \frac{\partial}{\partial x_k}\left(\left(\frac{\mu_l}{\mathrm{Pr}} + \frac{\mu_t}{\sigma_\omega}\right)\frac{\partial \omega}{\partial x_k}\right) + S_\omega \tag{7}$$

Where, $\rho$, $u_i$, $p$, $H$ are the density, velocity components, pressure and total energy respectively and $\mu = \mu_l + \mu_t$ is the total viscosity; $\mu_l$, $\mu_t$ being the laminar and turbulent viscosity and *Pr* is the Prandtl number.

The source terms are,

$$S_k = \tau_{ij}^* \frac{\partial u_i}{\partial x_j} - \beta^* \rho \omega k \tag{8}$$

$$S_\omega = \frac{\gamma}{\nu_t}\tau_{ij}^* \frac{\partial u_i}{\partial x_j} - \beta\rho\omega^2 + 2(1 - F_1)\sigma_{\omega 2}\frac{\rho}{\omega}\frac{\partial k}{\partial x_j}\frac{\partial \omega}{\partial x_j} \tag{9}$$

The model constants are obtained through the following blending relation:

$$ø = F_1 ø_1 + (1 - F_1) ø_2 \tag{10}$$

Where $ø_1$ , $ø_2$ and $ø$ , respectively, represent any constant in the *k–ω* model, the *k–ε* model, and the SST model. The blending function ($F_1$), that controls the switch between the *k–ω* and *k–ε* models takes the form

$$F_1 = \tanh(arg_1^4) \tag{11}$$

The argument is defined as,

$$arg_1 = \min\left[\max\left\{\frac{\sqrt{k}}{0.09\ \omega y}, \frac{500\nu}{y^2\omega}\right\}, \frac{4\rho\sigma_{\omega 2} k}{y^2\ CD_{k\omega}}\right] \tag{12}$$

Where *y* is the distance to the wall and $CD_{k\omega}$ the positive portion of the cross-diffusion terms expressed as

$$CD_{k\omega} = \max\left[2\rho\sigma_{\omega 2}\frac{1}{\omega}\frac{\partial k}{\partial x_j}\frac{\partial \omega}{\partial x_j}, 10^{-20}\right] \tag{13}$$

The constants in the Wilcox *k–ω* model are

$\sigma_{k1} = 0.85$, $\sigma_{\omega 1} = 0.5$, $\beta_1 = 0.075$, $\beta^* = 0.09$, $k = 0.41$, $\gamma_1 = \beta_1/\beta^* - \sigma_{\omega 1} k^2/\sqrt{\beta^*}$

and the constants in the standard *k-ε* model are

$\sigma_{k2} = 1.0$, $\sigma_{\omega 2} = 0.856$, $\beta_2 = 0.0828$, $\beta^* = 0.09$, $k = 0.41$, $\gamma_2$. $= \beta_2/\beta^* - \sigma_{\omega 2} k^2/\sqrt{\beta^*}$

### 3.3. Combined combustion model (CCM)

The CCM model computes the minimum of the eddy dissipation and finite rate chemistry models (i.e., *ED/FRC* model) reaction rate. The single-step global kinetics scheme is adopted in light of its simplicity and reasonably accurate modeling of the burned gas containing completely oxidized species of ethylene fuel. The scheme for ethylene-oxidation involves the following one step (global step) reaction with five species:

$$C_2H_4 + 3(O_2 + 3.\ 345N_2) \rightarrow 2CO_2 + 2H_2O + 10.\ 035N_2 \tag{14}$$

***ED model:*** The effect of turbulent mixing on combustion is taken into account by means of the eddy-dissipation model (*EDM*) proposed by Magnussen and Hjertager [20]. In this model, the chemical reaction is fast relative to the transport process in the flow. When, reactants mix at the molecular level they instantaneously form products. The model assumes that the reaction rate may be related directly to the time required to mix reactants at molecular level. In turbulent flows,

this mixing time is dictated by the eddy properties and therefore the burning rate is proportional to the rate at which turbulent kinetic energy is dissipated i.e., reaction rate $\sim\varepsilon/k$, where k is the turbulent kinetic energy and $\varepsilon$ is its rate of dissipation. The reaction rate associated with turbulent mixing, is given by the minimum of the following three rates

$$\dot{w}_{c_2H_4,edm} = -A_{edm}\frac{\varepsilon}{K}\ \min\left\{\left[\chi_{C_2H_4}\right], \frac{1}{\nu}*[\chi_{02}], B_{edm}*\frac{1}{1+\nu}[\chi_p]\right\} \quad (15)$$

where $[\chi_{C_2H_4}]$, $[\chi_{02}]$, and $[\chi_p]$ represent the molar concentrations of the fuel, oxygen, and product species, respectively, $A_{edm}$ and $B_{edm}$ are empirical constants taken to be 4.0 and 0.5, respectively, $\varepsilon/k$ the fluctuation frequency, and $\nu$ the stoichiometric oxygen to fuel mass ratio.

***FRC model*:** In this model the kinetic rate of change of any species in a reaction is generally described by Arrhenius expression involving an exponential dependence on temperature and power law dependence on the concentrations of the reacting chemical species. The rate of reaction of $\dot{w}_{C_2H_4,frc}$ (in kg mol/m$^3$ s) is given by the expression [21].

$$\dot{w}_{c_2H_4,frc} = -A_1 * T^{\delta} * \exp\left(\frac{-E_a}{R_u T}\right) * [\chi_{C_2H_4}]^{0.1} * [\chi_{02}]^{1.65} \quad (16)$$

The pre-exponential factor ($A_1$), temperature exponent ($\delta$) and activation energy ( $E_a$) are taken as $3.8e+12$ (kmol/cm$^3$)$^{-0.75}$/s, 0.0 and 30 kcal/mol respectively in present simulation.

The reaction rate is then determined from the minimum of the mixing and kinetic net rate by CCM and is expressed as

$$\dot{w}_{C_2H_4,\ \text{combined}} = \min\left[\dot{w}_{C_2H_4,\ edm}, \dot{w}_{C_2H_4,\ frc}\right] \quad (17)$$

### 3.4. Heat flux modelling near the wall

In present research work, Launder and Spalding [22] wall-function approach is used for prediction of heat flux near wall. In the log-law region, near wall tangential velocity ($U_t$) is related to wall-shear-stress ($\tau_\omega$), by means of a logarithmic relation. In the wall-function approach, the viscosity affected sublayer region is bridged by employing empirical formulas to provide near-wall boundary conditions for the mean flow and turbulence transport equations. These formulas connect the wall conditions (e.g., the wall-shear-stress) to the dependent variables at the near-wall mesh node which is presumed to lie in the fully-turbulent region of the boundary layer.

The logarithmic relation for the near wall velocity is given by:

$$u^+ = \frac{U_t}{u_\tau} = \frac{1}{\kappa}\ln(y^+) + C \quad \text{where } y^+ = \frac{\rho\Delta n u_\tau}{\mu} \quad \text{and}$$
$$u_\tau = \left(\frac{\tau_\omega}{\rho}\right)^{\frac{1}{2}} \quad (18)$$

$u^+$ is the near wall velocity, $u_\tau$ is the friction velocity, $\rho$ is density, $U_t$ is the known tangent velocity to the wall at a distance of $\Delta n$ from the wall, $y^+$ is the dimensionless distance from the wall, $\kappa$ is the von Karman constant and $C$ is a log-layer constant depending on wall roughness.

The heat flux at the wall is modeled using the thermal law-of-the-wall function approach by Kader [23]. The heat flux distribution ($q_w$) near-wall is calculated as follows:

$$q_w = \frac{\rho C_p u_\tau}{T^+}(T_w - T_f) \quad (19)$$

where, $T^+ = \frac{T}{T_w} = \Pr * y^+ * e^{(-\Gamma)} + \left[2.12 * ln(y^+) + \beta\right] * e^{(-\Gamma)}$

$\beta = \left(3.85 Pr^{1/3} - 1.3\right)^2 + 2.12 * ln(Pr)$, $Pr = \frac{\mu * C_p}{\lambda}$, $u_\tau = \left(\frac{\tau_\omega}{\rho}\right)^{1/2}$

$\Gamma = \frac{0.01 * (\Pr * y^+)^4}{1 + 5 * \Pr^5 * y^+}$ and $y^+ = \frac{\rho * \Delta n * u_t}{\mu}$.

## 4. Results and discussion

Since the residence time in the device is of the order of milliseconds, one of the major challenges for hypersonic vehicle designer is to properly mix the high-speed air with the fuel to induce efficient and rapid combustion. In the present work, numerical simulations of nonreacting with and without fuel injection and reacting flow with combustion are carried out to study mixing and combustion flow behavior inside hypersonic cruise vehicle with ethylene fuel for two equivalence ratios of 0.6 and 0.8 respectively.

### 4.1. Computational domain and grid generation

Taking the advantage of pitch plane symmetry (along the width) of the geometry only half of the vehicle geometry is considered for the simulation. The inlet boundary is placed at one width ($W$) distance upstream of the vehicle nose and the outlet boundary is placed $8W$ distance of vehicle base. Multi-block structured (i.e., total number of blocks about 8950 for whole domain) hexahedral grids are made using *ANSYS ICEM-CFD* [18] for the entire computational domain. Adequate care is taken in the preparation of grids for good quality ensuring the proper skewness and aspect ratio. The total grid distribution about 19.81 million cells (i.e., $601 \times 201 \times 164$ grid points along the flow direction, height and width of the cruise vehicle respectively) is generated for the computational domain of half cruise vehicle geometry.

The grids are fine near the vehicle internal and external (i.e., forebody, intake, combustor and SER nozzle regions) surfaces, leading edges of the struts and middle wall, trailing edge regions of the struts, near-wall regions, while relatively coarser grids are provided in the remaining portion of the computational domain. This helps to resolve the boundary layers well to achieve wall $y^+$ values as low as possible to capture flow feature accurately. Average $y^+ \sim 5$ is obtained for whole hypersonic vehicle including internal and external flows in the present simulations. Since, injected ethylene fuel ($C_2H_4$) is in gaseous form, resolution of grids at injection holes is very much necessary. A grid distribution of $8 \times 8$ is provided at each injection location to capture fuel injections areas accurately. Typical grid distribution on various planes of cruise vehicle and injection holes is shown in Fig. 2. In the present simulation, $X$-axis is taken along the length of vehicle (i.e., axial direction), while, $Y$ and $Z$-axis are chosen along the width (i.e., yaw direction) and height (i.e., pitch direction) of the cruise vehicle respectively, with the origin being placed at intersection point of symmetry plane and vehicle nose.

### 4.2. Inflow and boundary conditions

Nonreacting (cold flow) and reacting flow simulations are carried out for altitude of 31 km and Mach number of 6.1 with angle of attack of 4° at two different equivalence ratios of 0.6 and 0.8 respectively. Ethylene fuel is injected in gaseous form in sonic speed. Following Ref [24], dynamic viscosity, molecular weight, density, and thermal conductivity of ethylene fuel are $1.027 \times 10^{-5}$ Pa s, 28.05 kg/kmol, 18.005 kg/m$^3$, 0.0205 W/m K respectively. Specific heat at constant pr, $C_p$ (J/kg K) is considered to vary with temperature. Supersonic inflow conditions are provided at the inflow planes of free-stream and fuel entry conditions and all the flow properties are kept constant in these planes. Two different wall conditions, i.e. adiabatic wall ($q_w = 0.0$) and isothermal wall ($T_w = 1000$ K) boundary conditions are imposed on the walls depending on the requirement of thermal characteristics

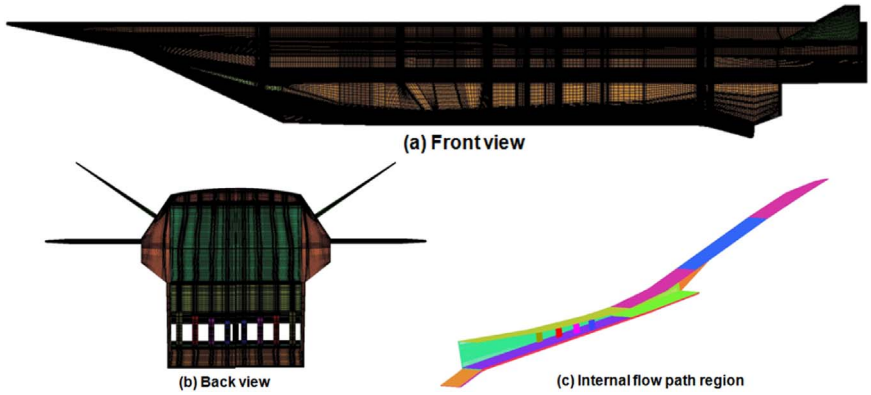


**Fig. 2.** Grid distribution at different planes of around hypersonic cruise vehicle.

on the walls. Supersonic outflow boundary condition is applied at the exit of the computational domain. Symmetry boundary condition is imposed at the symmetry plane. The symmetry plane boundary condition imposes constraints which 'mirror' the flow on either side of it. The normal velocity component ($U_n$) at the symmetry plane boundary is set to zero and the scalar variable gradients normal to the boundary ($\partial\phi/\partial n$) are also set to zero. The global mass, momentum, and energy imbalance less than 0.1% between outlet and inlet of the computational domain have been considered as the convergence criteria.

### 4.3. Flow field analysis in nonreacting flow

#### 4.3.1. Nonreacting flow without fuel injection

Numerical simulation is carried out for angle of attack ($\alpha$) of 4°. The simulation captured all essential flow features of hypersonic flow, i.e., bow shock, oblique shocks and series of reflecting shocks inside the intake and combustor which is shown through the representation of Mach number and density gradient in Fig. 3. The high-speed air flow is compressed at the vehicle forebody and intake and then passes through the scramjet combustor. The forebody provides the initial external compression and contributes to the drag and moments of the vehicle. The intake provides the final compression of high speed air to provide the inflow conditions for the scramjet engine. A series of oblique shocks are generated from the vehicle body under surface and cowl surface as the flow proceeds through the intake towards combustor as shown in the density gradient in Fig. 3(b). The computed pressure and temperature distribution in the internal flow path (at $Z/W=-0.74$ plane) is shown in Fig. 4. The internal flow structures are highly three dimensional and the strut generated shocks are clearly visible from the increased pressure and temperature in the flow path. Pressure and temperature reduce in the downstream region due to flow expansion. The net drag force acting on the cruise vehicle is 335 N/kg/s (for full vehicle) whereas, net drag from four pairs of struts is 210 N/kg/s for cold flow conditions.

#### 4.3.2. Nonreacting flow with fuel injection – mixing characterization

For this study, ethylene fuel is injected with equivalence ratio ($\phi$) of 0.6 from struts transversely into supersonic air flow. Ethylene fuel mass fractions ($Y_{C2H4}$) at various axial locations (i.e., $X/W=2.24$, 2.86, 3.51, 4.19, 4.94 and 5.70) are shown in Fig. 5. Some of the regions do not mix properly which is shown with red color arrow on the figure. To get more details of mixing characteristics, composite picture of streamline colored with fuel mass fraction and density gradient is plotted in Fig. 5(b) and (c). Ethylene fuel streamlines are diverted towards core regions of combustor due to interaction of strut generated oblique shocks and side wall boundary layer of the combustor. The regions in between 3rd and 4th struts show less mixing of air with fuel.

The axial distribution of mixing efficiency and total pressure loss is shown in Fig. 6. The mixing efficiency of the fuel ($\eta_m$) is defined as the fraction of ethylene mass that could be burned (at given state of mixing in case of infinitely fast chemistry) in relation to the total amount of ethylene fuel injected inside the combustor. To evaluate the mixing efficiency ($\eta_m$) along the combustor flow path, the following expression [25] is used.

$$\eta_m(x)=\frac{\int \alpha \rho_{gas} Y_{C2H4} u dA}{\dot{m}_{C2H4}}$$

$$\text{with} \quad \alpha = \begin{cases} \dfrac{1}{\varnothing_L}: & \varnothing_L \geq 1, \\ 1: & \varnothing_L < 1 \end{cases} \tag{20}$$

Where, $\rho_{gas}$ is the gas density, $Y_{C2H4}$ is the mass fraction of ethylene, $A$ is the cross-sectional area and $u$ is the axial velocity. Here, $\varnothing_L$ is the local equivalence ratio and is defined as:

$$\varnothing_L=3*\frac{M_{O_2}}{M_{C_2H_4}}\frac{Y_{C_2H_4}}{Y_{O_2}} \tag{21}$$

Where, $M_{C_2H_4}$ and $M_{O_2}$ are the molecular weights of ethylene and oxygen respectively, and $Y_{O_2}$ is the mass fraction of oxygen.

Mixing efficiency($\eta_m$)=1 indicates a perfect mixing, whereas, $\eta_m=0$ represents no mixing of fuel and oxidizer. The mixing efficiency is more behind the strut regions where fuel is injected. The maximum mixing efficiency of about 98% is obtained at the exit of the combustor (i.e., $X/W=5.71$). Total pressure loss ($P_{0L}$) is defined as the ratio of difference between total pressures at free stream

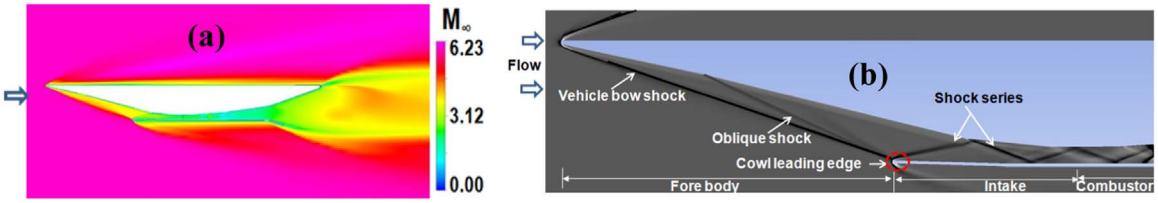


**Fig. 3.** Computed (a) Mach number and (b) Density gradient at $Y/W=0.172$ from symmetry.

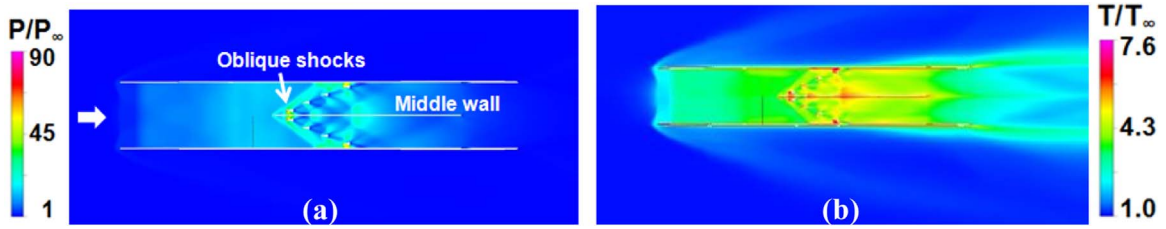


**Fig. 4.** (a) Static pressure and (b) Static temperature distribution at internal flow path of cruise vehicle at plane passing through $Z/W=-0.74$.

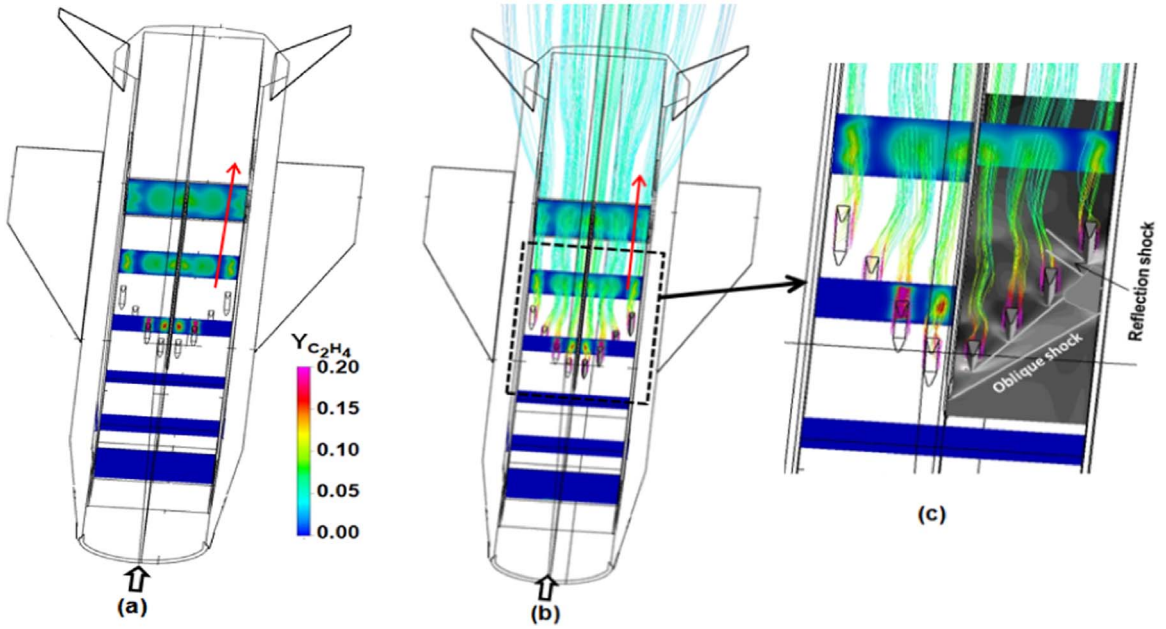


**Fig. 5.** Ethylene fuel mass fractions, (a) Various axial locations (X/$W$=2.24, 2.86, 3.51, 4.19, 4.94 and 5.70), (b) Contour at different axial locations and streamline color with $Y_{C2H4}$ and (c) Expanded view of composite picture for shock structure and streamline at struts regions. (For interpretation of the references to color in this figure legend, the reader is referred to the web version of this article.)

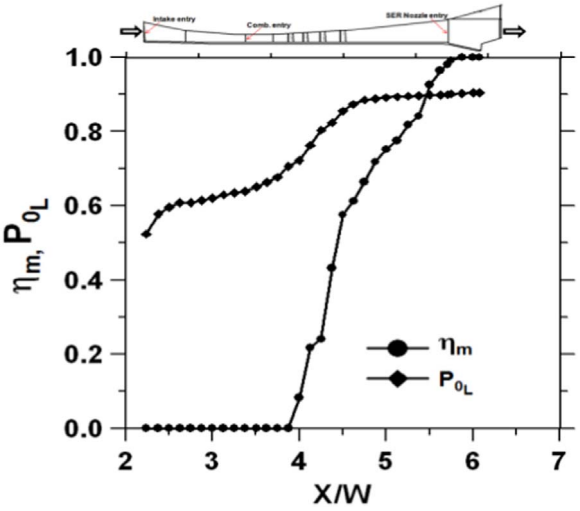


**Fig. 6.** The axial distribution of mixing efficiency and total pressure loss.

entry plane to local plane at any location inside the cruise vehicle by free stream total pressure. Hence, by definition of TPL is expressed as follows;

$$P_{0_{L(x)}}=\left(1-\frac{P_{0_x}}{P_{0_\infty}}\right)*100 \tag{22}$$

Where $P_{0_x}$ and $P_{0_\infty}$ are local total pressure (mass average) at any axial cross section and free stream entry total pressure (mass average) respectively. $P_{0L}$ continuously increases along the length of the cruise vehicle internal flow path due to multiple shock structure. The net total pressure loss is 52%, 65% and 90% at intake, combustor and *SER* nozzle entries respectively.

### 4.4. Reacting flow results

Reacting flow simulations are performed for two equivalence ratios ($\phi$) of 0.6 and 0.8 to study the flow field characteristics and also estimate heat flux distribution on the walls of the hypersonic cruise vehicle.

#### 4.4.1. Flow field characterization with $\phi=0.6$

The distributions of Mach number, pressure, temperature and mass fractions of carbon dioxide ($CO_2$), water vapor ($H_2O$) oxygen ($O_2$), ethylene vapor ($C_2H_4$) are provided to represent the flow characteristics. Net performance of cruise vehicle in terms of combustion efficiency, net thrust (combustor and *SER* nozzle thrusts), specific impulse and drag values are provided to understand hypersonic vehicle behavior under reacting flow.

Mach number distributions at two planes, (i.e., mid-width at $Y/W=0.172$ and mid-height at $Z/W=-0.74$ respectively) are shown in Fig. 7. Large subsonic flow regions are observed adjacent to the side wall and behind the struts (Fig. 7(b)), which is due to combustion of ethylene fuel. The cross sectional views of Mach number and $CO_2$ mass fraction distribution at various axial locations are shown in Fig. 8. Subsonic regions adjacent to strut 2 ($X/W=4.19$)

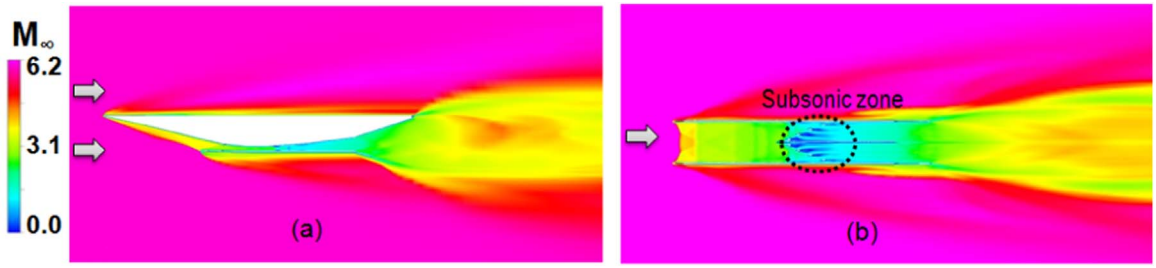


**Fig. 7.** Mach number contour at plane passing through (a) $Y/W=0.172$ and (b) $Z/W=-0.74$.

and 3 ($X/W=4.50$) regions have been shown clearly (zoomed view) in the figure. Supersonic regions are represented by color; whereas, uncolored portions of the cross section represent the subsonic zone. Various shock interactions from combustor walls and struts and combustion of ethylene fuel with incoming air is reducing the Mach number in the strut wake region significantly. Static pressure and static temperature distribution in the internal flow path at $Z/W=-0.74$ is shown in Fig. 9. Both pressure and temperature increase in these regions due to combustion of fuel and heat release from the reactions. Comparing the values of Mach number and static pressure with nonreacting results (Fig. 4) in the internal flow path, we can observe significant differences in the flow behavior. The pressure rise in the combustor due to reaction does not affect the flow upstream.

Mass flow average of Mach number, static pressure, static temperature and $P_{0L}$ along the length of the internal flow regions of cruise vehicle (i.e., intake, combustor and SER nozzle) are plotted in Fig. 10 (a) and (b) respectively. Average Mach number is found to reduce from 3.61 at intake entry to about 1.0 at $X/W=4.43$, which is due to shock interaction from various walls of the combustor and mixing and combustion of ethylene fuel with dry air. In the divergent part of the combustor and SER nozzle, Mach number increases to 2.31 at the trailing edge of *SER* nozzle cowl at $X/W=6.13$ (shown in Fig. 10 (a)). Static pressure ($P/P_\infty$) and temperature ($T/T_\infty$) are found to increase from 10.1 and 2.5 at intake entry to about 137 and 9.65 at the struts region respectively due to combustion of fuel with surrounding air (Fig. 10(a)). $P_{0L}$ increases along the length of the internal flow of cruise vehicle as shown in Fig. 10(b). About 51% of $P_{0L}$ is observed in forebody due to compression of high speed flow with ramps. Another 15% and 25% of $P_{0L}$ are found due to internal compression at intake and heat release in combustor respectively. Total pressure availed at the exit of the combustor and at trailing edge of *SER* nozzle cowl are 7.6% and 7.0% of the vehicle free stream value respectively, showing a net $P_{0L}$ of 93% in the whole cruise vehicle which is about 11% more compared to the nonreacting flow condition.

The reaction pattern in the combustor is depicted through species mass fraction of $CO_2$, $C_2H_4$ and $O_2$ distribution at various axial locations ($X/W=2.2$, 2.9, 3.5, 4.2, 4.9, 5.7 and 6.4) in Fig. 11 (a) to (c) respectively. Reaction zones are seen to cover whole width of the combustor from the axial location of $X/W=4.94$ onwards. Small amount of un-burnt ethylene fuel is observed adjacent to the side wall regions of the combustor (Fig. 11(b)). Considerable amount of $Y_{O2}$ (Fig. 11(c)) is found to remain un-burnt in between the 3rd and 4th struts regions, which is due to the fact that sufficient amount of fuel is not available in these regions (only 60% of the stiochimetric amount of fuel is injected in the combustor).

The cruise vehicle wall pressures distribution along the flow direction at the centerbody and cowl surfaces are compared between nonreacting and reacting flows in Fig. 12. Initially, high peak vehicle under surface wall pressure is observed at vehicle nose region due to bow shock generated by high speed flow. Wall pressure slightly increases in ramp surfaces due to compression of

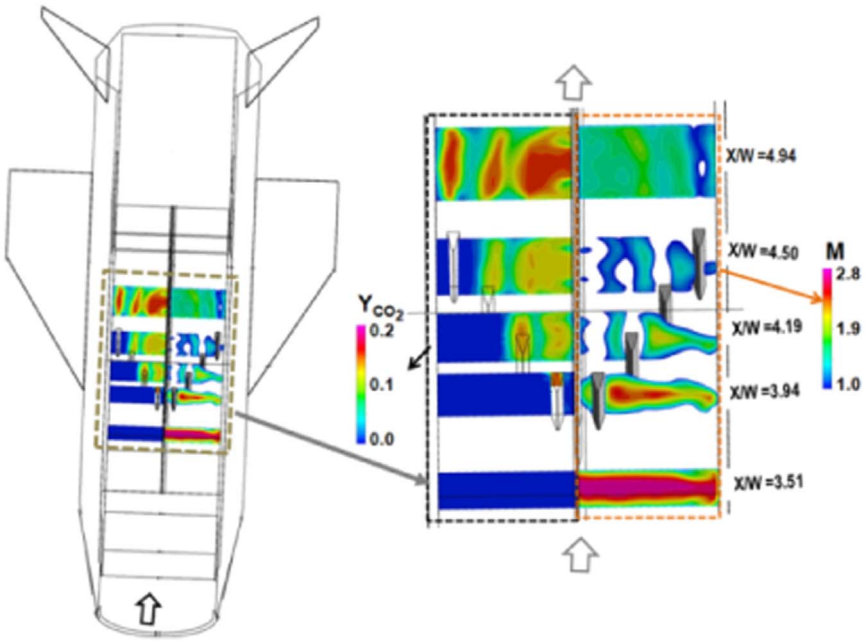


**Fig. 8.** Mach number and $CO_2$ mass fraction contour at various axial planes. (For interpretation of the references to color in this figure, the reader is referred to the web version of this article.)

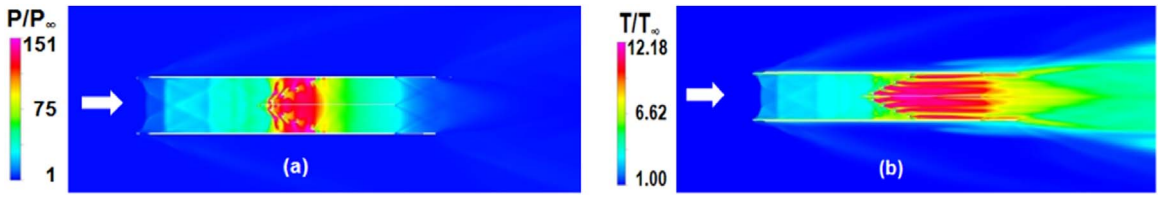


**Fig. 9.** The contour of (a) static pressure and (b) static temperature distribution in the internal flow path at $Z/W=-0.74$.

high speed flow within a region of $0.25 < X/W < 2.7$. Wall pressure increases after $X/W > 3.1$ due to internal compression of flow. At the divergent portion of the combustor of cruise vehicle (i.e., $X/W > 4.4$), wall pressures continually decrease due to flow expansion. For reacting case, wall pressure increases due to combustion of ethylene fuel till $X/W=4.43$. Almost similar type of pressure distribution is observed along the intake cowl surface.

Overall forces of the cruise vehicle is calculated from the simulation results and presented in Table 1 (negative sign indicates force acting in the direction opposite to drag force, which is considered as thrust). The computed positive thrust – drag margin, combustion efficiency and specific impulse are 159 N/kg/s, 94% and 1538 s respectively.

*4.4.2. Effect of equivalence ratio on vehicle performance*

Simulation is carried out with $\phi=0.8$ to study the effect of equivalence ratio ($\phi$) on hypersonic vehicle performance. Axial distributions of average Mach number and static temperature are compared for these two equivalence ratios in Fig. 13 (a) and (b). Lower Mach number is found at reaction intense zones in case of higher equivalence ($\phi=0.8$) ratio due to more heat release from combustion. For $\phi=0.8$, average Mach number has become subsonic in between $4.22 < X/W < 4.58$ with a minimum Mach number of 0.92 at $X/W=4.53$ in comparison to the subsonic region of $4.392 < X/W < 4.53$ with a minimum Mach number of 0.97 at $X/W=4.5$ for $\phi=0.6$. Static temperature is found more in case $\phi=0.8$ due to more reaction of ethylene fuel with air (Fig. 12(b)). Net vehicle thrust is increased by 44.4% and combustion efficiency is reduced by 8% for $\phi=0.8$. The computed specific impulse for 0.8 equivalence ratio is 1316 s. In spite of higher achieved thrust, less combustion efficiency and higher fuel consumption is responsible for lower specific impulse for $\phi=0.8$.

*4.4.3. Estimation of heat flux on cruise vehicle at $\phi=0.6$*

Since, the estimation of wall heat flux is very sensitive to grid size, heat flux estimation methodology was validated [26] for experimental results of convective heat transfer phenomena in a convergent – divergent nozzle [27]. The same authors has simulated Back et al [27] experimental condition with two different grids of 0.55 million (coarse grid) and 0.83 million (fine grid) with average $y^+$ of 2. It is observed that minimum 1st grid spacing of 10 μm is required to predict the wall heat flux values correctly adjacent to the wall. The computed convective heat flux data in the nozzle wall with different grids are compared with experimental value in Fig. 14 and the computation matches with experiment very nicely.

Also, an estimate of the error due to grid in the form of Grid Convergence Index (*GCI*) is presented in Fig. 14. Roache [28] proposed a grid convergence index (*GCI*) as an error based on uncertainty estimate of the numerical solution as,

$$GCI=F_s\frac{|\Psi|}{(h_2/h_1)^{\in}-1}$$

Here, $h$ is the order of grid spacing, $\in$ is the order of accuracy of numerical scheme and $F_s$ is a factor of safety. $\Psi$ is the relative difference, represented as $\Psi=\frac{f_1-f_2}{f_1}$, where $f$ is any quantity of interest. Suffixes *1* and *2* refer to the fine and coarse grid solution respectively. Roache [29] suggested $F_s = 3$ for minimal of two grid calculations. For the present calculation, $\in$ is equal to 2 with $h_2/h_1$ equal to 2, *GCI* is order of $\Psi$. In the present calculation, top wall convective heat flux is taken as the parameter of interest and peak value of GCI in the whole computational domain is about 4%. The same procedure of error estimate was adopted in different simulations [30,15].

*RANS* simulations with fine resolution of wall boundary layer ($y^+ \sim 1$), gives directly the wall heat flux for a fixed wall temperature. Heat flux obtained from one fixed wall temperature is not same for different wall temperatures. A new 'isothermal method' is explained in Ref. [31] where wall heat flux ($\dot{q}_{cw}$) is calculated based on fixed wall temperature ($T_{cw}$) and wall heat fluxes ($\dot{q}_w$) at other wall temperatures are scaled to the local wall temperature utilizing adiabatic wall temperature ($T_{aw}$) as given below,

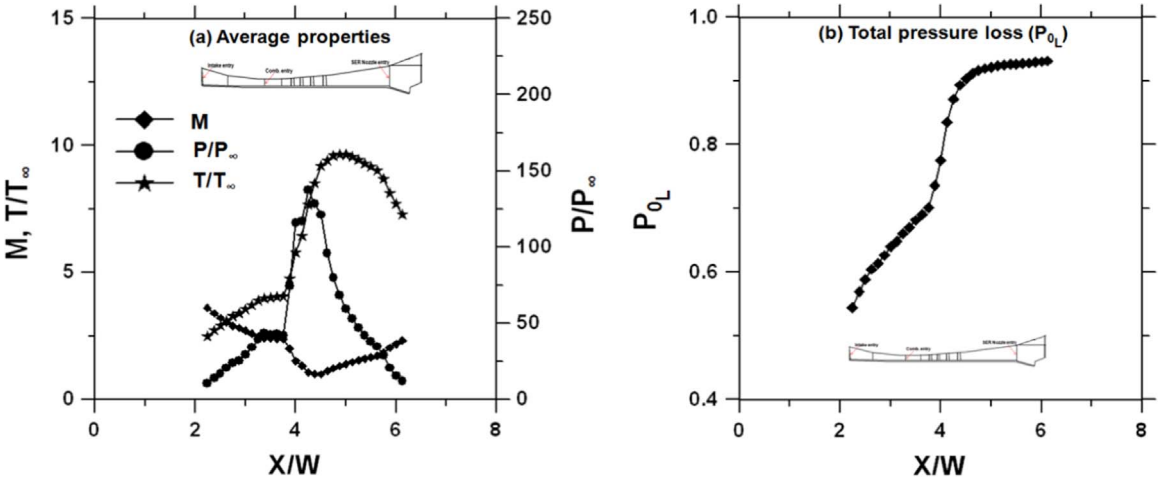


**Fig. 10.** Axial distributions of different flow parameters along the combustor length.

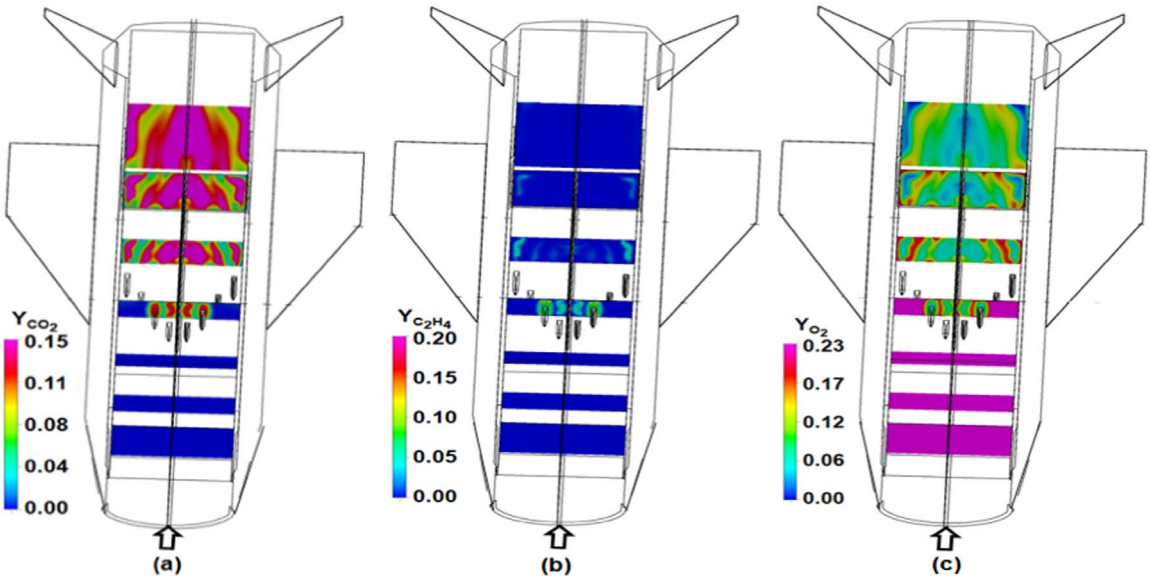


**Fig. 11.** Species distribution at various axial locations along the flow direction; **(a) $Y_{CO2}$, (b) $Y_{C2H4}$ and (c) $Y_{O2}$.**

Local wall heat flux $\dot{q}_w = \dot{q}_{cw} \times \left[\frac{T_{aw} - T_w}{T_{aw} - T_{cw}}\right]$

This 'isothermal method' requires one CFD simulation with isothermal wall and another CFD simulation with adiabatic wall. The validation of the methodology for different external and internal flow problems are presented in Ref. [31].

To study the thermal characteristics in the near wall regions, simulation is carried out considering isothermal wall condition ($T_w$) of 1000 K for all surfaces of the cruise vehicle for $\phi$=0.6. In the present computation, minimum grid spacing of 5 μm is maintained on all the walls of the vehicle. Wall pressure and wall shear stress distribution in the mid generator of vehicle under surface are compared between isothermal and adiabatic cases in Fig 15. As expected, the thermal boundary conditions at wall does not alter the pressure distribution; while, the wall shear distribution show higher values for isothermal case compared to adiabatic case. Convective heat flux distribution at various internal flow surfaces are shown in Fig. 16. Higher local heat flux values are observed at all the leading edges of the cruise vehicle (i.e., nose, wing, fin and cowl leading edges) because of oblique shocks generated due to hypersonic flow on cruise vehicle. Local heat flux increases in forebody and intake due external compression of high speed flow. Higher heat fluxes are also observed inside the combustor due to the combustion of ethylene fuel with surrounding air. Heat flux reduces at the last divergent portion of the combustor and SER nozzle due to the expansion of the supersonic flow.

**Table 1**
Hypersonic vehicle net performance.

| Various components | Value |
|---|---|
| Vehicle net axial force, N/kg/s | 159 |
| Combustor thrust, N/kg/s | 356 |
| SER Nozzle thrust, N/kg/s | 229 |
| Vehicle lift force, N/kg/s | 975 |
| Combustion efficiency, % | 94 |
| Specific Impulse, $I_{sp}$ (s) | 1538 |

Convective heat flux distribution along the flow direction on a line generated at $Y/W$=0.172 on intake cowl and vehicle body under surface is shown in Fig.17. Higher heat flux values are observed at vehicle nose and intake cowl leading edge due to strong

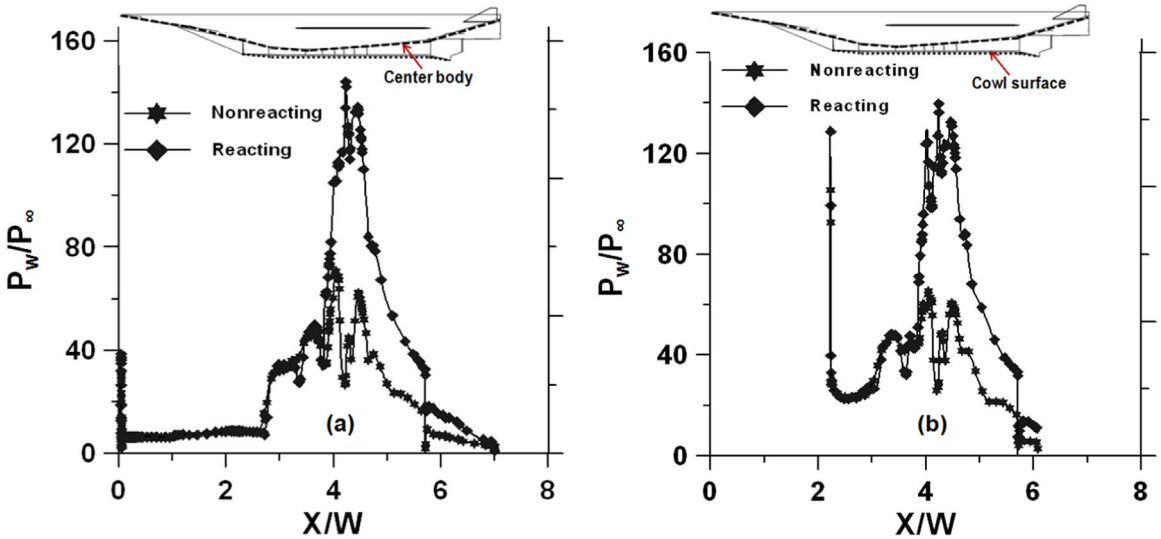


**Fig. 12.** Comparison of wall pressure distribution at $Y/W$=0.172; (a) Center body (b) cowl surface.

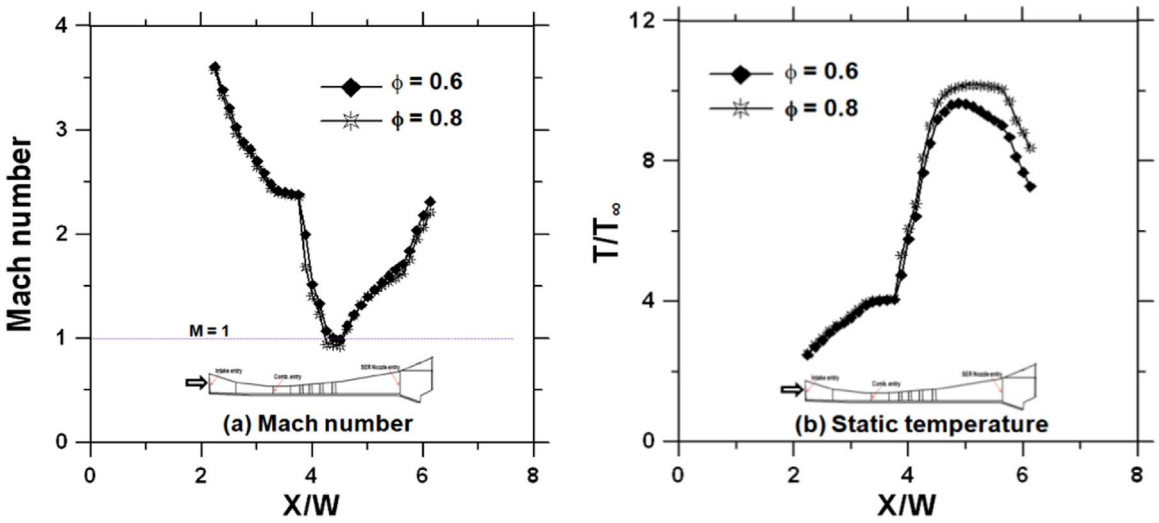


**Fig. 13.** Comparison of mass flow average property distribution for two different equivalence ratio.

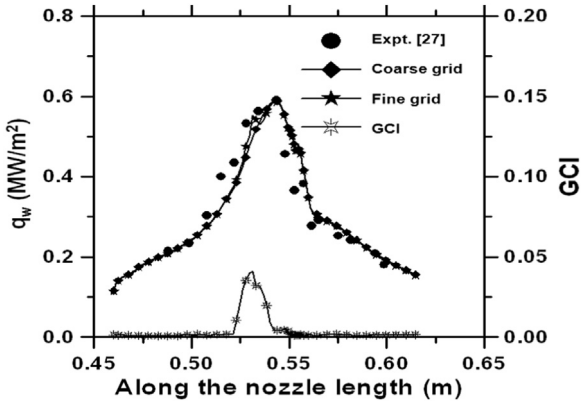


**Fig. 14.** Comparison of axial distribution of wall heat flux with different grids with experimental value [27] and GCI distribution.

oblique shock and higher wall shear. The combustor strut regions also experience higher heat flux due to more heat release from the combustion of ethylene fuel. The local peak heat flux ($q_w/q_{w,max}$ where $q_{w,max}$ is maximum heat flux at the leading edge of struts) values of 0.27, 0.67 and 0.48 are observed at vehicle nose, intake cowl leading edge and combustor strut regions respectively for isothermal wall temperature $T_w = 1000$ K. In divergent portion of combustor and *SER* nozzle regions (i.e., $4.04 < X/W < 7$), heat flux values continuously decrease due to flow expansion.

## 5. Conclusions

Tip-to-tail flow field of an ethylene fueled hypersonic air-breathing vehicle is explored numerically by solving 3-D *RANS* equations along with *SST-k-ω* turbulence model and single step global chemical reaction for ethylene fuel using commercial CFD software. To study the interaction between aerodynamics and propulsion, both nonreacting hypersonic flow fields in vehicle forebody, intake, fuselage, tail fins and reacting flow field in the scramjet combustor are simulated simultaneously. Simulations captured all the essential features of the flow field including shock impingements and reflection waves in the vehicle undersurface, intakes and combustor top and bottom walls. The interaction of various waves inside the flow duct causes significant non-uniformity of the flow at the inlet of the combustor.

Various thermo-chemical parameters (distribution of $CO_2$, $H_2O$, unused $O_2$ and unburnt ethylene mass fraction), pressure and

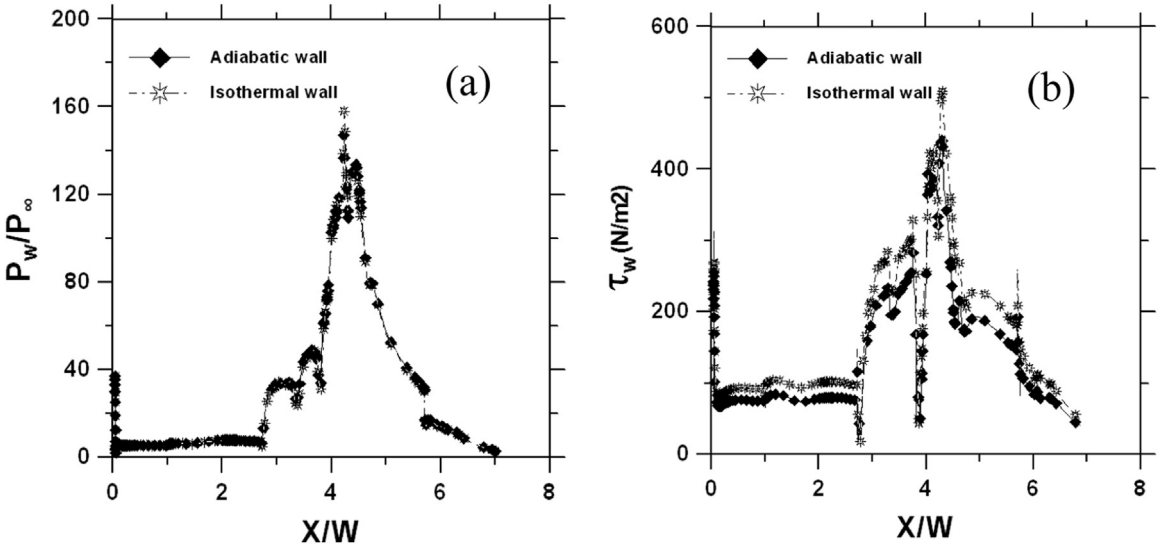


**Fig. 15.** (a) Wall pressure and (b) shear stress distribution in the vehicle under surface between adiabatic wall and isothermal wall boundary conditions.

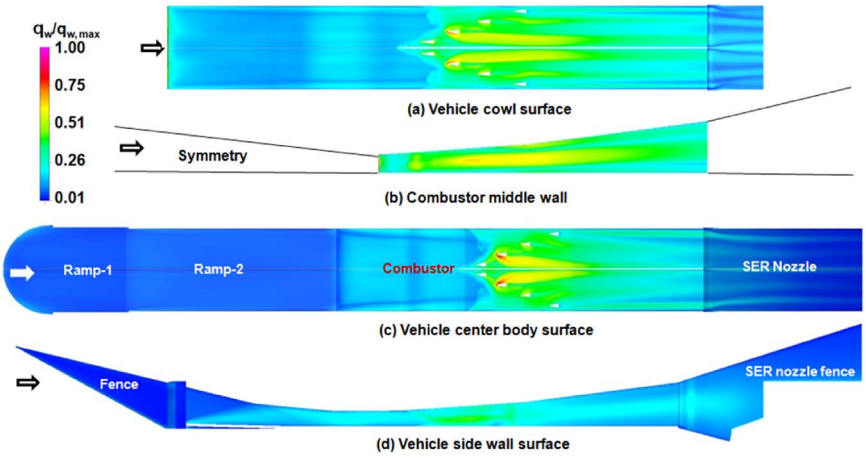


**Fig. 16.** Local heat flux distribution on internal flow surface of cruise vehicle.

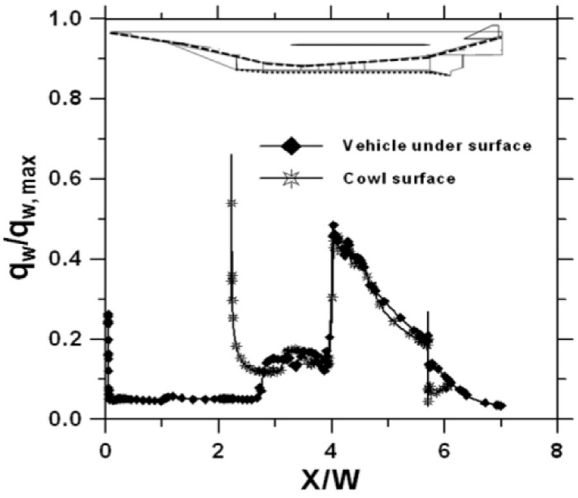


**Fig. 17.** Heat flux distribution on two different surface of cruise vehicle at $Y/W=0.172$.

viscous forces on various components, wall pressure distribution etc. are analyzed to estimate the overall force balance and the vehicle performance at different equivalence ratios. Net vehicle thrust is increased by 44.4% and combustion efficiency is reduced by 8% for higher equivalence ratio ($\phi=0.8$) compared to that of lower equivalence ratio ($\phi=0.6$). In spite of higher achieved thrust, less combustion efficiency and higher fuel consumption is responsible for lower specific impulse for higher equivalence ratio. Both isothermal and adiabatic flow field of the vehicle is analyzed to estimate convective heat flux distribution in different vehicle surfaces for thermostructural analysis. The vehicle nose, intake cowl leading edge and combustor strut regions experience high convective heat flux rates.

## Acknowledgment

The authors would like to acknowledge the help of the project team, HSTDV of DRDL for providing the cruise vehicle geometry and necessary input conditions for the simulation during the course of the work. The work did not receive any fund from any sources.

## References

[1] E.T. Curran, Scramjet Engines: the first forty years, J. Propuls. Power 17 (6) (2001) 1138–1148.
[2] In: E.T. Curran, S.N.B. Murthy (Eds.) Scramjet propulsion. Progress in Astronautics and Aeronautics AIAA 2001;Washington, DC.
[3] P. Manna, R. Behera, D. Chakraborty, Design and analysis of liquid fueled strut based scramjet combustor – a CFD approach, J. Propuls. Power 24 (2) (2008) 274–281.
[4] C.R. McClintona, V.L. Rauscha, R.J. Shawb, U. Methac, C. Nafteld, Hyper-X: foundation for future hypersonic launch vehicles, Acta Astronaut. 57 (2005) 614–622.
[5] R.T. Voland, L.D. Huebner, C.R. McClinton, X-43A hypersonic vehicle technology development, Acta Astronaut. 59 (2006) 181–191.
[6] M.C. Rondeau, R.T. Jorris, X-51 A Scramjet demonstrator program: Waverider ground and Flight test, SETE$ 44th international/SETP southwest Flight test Symposium, 28 Oct–1 Nov, 2013, Ft Worth, TX.
[7] H. Sakurai, M. Kobayasi, I. Yamazaki, M. Shirouzu, M. Shirouzu, Development of the hypersonic flight experimental vehicle, Acta Astronaut. 40 (2–8) (1997) 105–112.
[8] I. Fedioun, E. Orlik, Boundary Layer Transition on the LEA Hypersonic Vehicle Forebody, 2012, AIAA 2012-5864.
[9] S. Pannerselvam, V. Thiagarajan, A.T.K. Ganesh, J.J. Geetha, V. Ramanujachari, Prahlada, Airframe Integrated Scramjet Design and Performance Analysis. ISABE Paper no. 2005-1280, 2005.
[10] C. Chandrasekhar, V. Ramanujachari, T. Kishen, Kumar Reddy, Evaluation of kerosene fuelled scramjet combustor using a combination of cooled and uncooled Strut, Def. Sci. J. 64 (1) (2014) 5–12.
[11] V. Ramanujachari, C. Chandrasekhar, V. Satya, S. Panneerselvam, Experimental investi-gations of a strut based scramjet combustor using kerosene fuel, in: Proceedings 7th Asia-Pacific Conference on Combustion, National Taiwan University, Taipei, Taiwan, 24–27 May, 2009, Paper ID 10161.
[12] P. Manna, M. Dharavath, P.K. Sinha, D. Chakraborty, Optimization of a flight-worthy scramjet combustor through CFD, Aerosp. Sci. Technol. 27 (2013) 138–146.
[13] Malsur Dharavath, P. Manna, Debasis Chakraborty, Effect of turbulence models and spray parameters on kerosene fuelled scramjet combustor, J. Aerosp. Sci. Technol. 67 (3) (2015) 369–383.
[14] C.J. Tam, K.U. Hsu, M.R. Gruber, et al. Fuel/air mixing characteristics of strut injections for scramjet combustor applications, in: Proceedings 26th AIAA Applied Aerodynamics Conference, 18–21 August 2008, Honolulu, Hawaii. AIAA 2008-6925.
[15] Malsur Dharavath, P. Manna, Debasis Chakraborty, Study of mixing and combustion in scramjet combustor with ethylene fuel through CFD, Acta Astronaut. 117 (2015) 305–318.
[16] Malsur Dharavath, P. Manna, Debasis Chakraborty, Computational fluid dynamics simulation of tip to tail for hypersonic test vehicle, J. Propuls. Power 31 (5) (2015) 1370–1379, http://dx.doi.org/10.2514/1.B35686.
[17] ANSYS ICEM-CFD-11, Installation and Overview, January 2007.
[18] ANSYS CFD, Release 14.5: Installation and Overview, January 2013.
[19] F.R. Menter, Two-equation eddy-viscosity turbulence models for engineering applications, AIAA J. 32 (8) (1994) 1598–1605.
[20] B.F. Magnussen, B.H. Hjertager, On mathematical modeling of turbulent combustion with special emphasis on soot formation and combustion, in: Proceedings of the Sixteenth Symp. (Int.) on Combustion, The Combustion Institute, 1976, pp. 719–725.
[21] C.K. Westbrook, F.L. Dryer, Simplified reaction mechanisms for the oxidation of hydrocarbon fuels in flames, Combust. Sci. Technol. 27 (1981) 31–43.
[22] B.E. Launder, D.B. Spalding, The numerical computation of turbulent flows, Comp. Methods Appl. Mech. Eng. 3 (1974) 269–289.
[23] B.A. Kader, Temperature and concentration profiles in fully turbulent boundary layers, Int. J. Heat. Mass. Transf. 24 (9) (1981) 1541–1544.
[24] P.M. Holland, B.E. Eaton, J.M. Hanley, A correlation of the viscosity and thermal conductivity data of gaseous and liquid ethylene, J. Phys. Chem. 12 (4) (1983).

[25] P. Gerlinger, P. Stoll, M. Kidler, F. Schneider, M. Aigner, Numerical investigation of mixing and combustion enhancement in supersonic combustor by strut induced streamwise vorticity, Aerosp. Sci. Technol. 12 (2008) 159–168.
[26] Malsur Dharavath, P. Manna, Debasis Chakraborty, Prediction of heat flux in a scramjet combustor with kerosene fuel through CFD", Paper No CP-37, in: Proceedings of 17th AeSI-CFD Symposium held at NAL, Bangalore, India, Aug. 11–12, 2015, pp. 168–177.
[27] L.H. Back, P.F. Massier, H.L. Gier, Convective heat transfer in a convergent–divergent nozzle, Technical Report 32-415, Jet Propulsion Laboratory, California Institute of Technology, Pasadena CA, 1965.
[28] P.J. Roache, Error Base for CFD, AIAA Paper 2003-0408, 2003.
[29] P.J. Roache, Verification and Validation in Computational Science and Engineering, Hermon Publishers, New Mexico, 1998.
[30] G. Aswin, Debasis Chakraborty, Numerical simulation of transverse side jet interaction with supersonic free stream, Aerosp. Sci. Technol. J. 14 (2010) 295–301.
[31] Anand Bhandarkar, Malsur Dharavath, M.S.R. Chandra Murty, P. Manna, Debasis Chakraborty, A novel CFD method to estimate heat transfer coefficient for high speed flows, Def. Sci. J. 66 (3) (2016) 203–209, http://dx.doi.org/10.14429/dsj/66.8873.